AIP | Journal of Applied Physics

Shock-induced consolidation and spallation of Cu nanopowders

L. Huang, W. Z. Han, Q. An, W. A. Goddard, and S. N. Luo

Citation: J. Appl. Phys. **111**, 013508 (2012); doi: 10.1063/1.3675174
View online: http://dx.doi.org/10.1063/1.3675174
View Table of Contents: http://jap.aip.org/resource/1/JAPIAU/v111/i1
Published by the American Institute of Physics.

Shock-induced consolidation and spallation of Cu nanopowders

L. Huang,[1,2,a)] W. Z. Han,[2] Q. An,[3] W. A. Goddard III,[3] and S. N. Luo[2,b)]
[1]*Physics Department, Harbin Institute of Technology, Harbin, Heilongjiang 150001, People's Republic of China*
[2]*Los Alamos National Laboratory, Los Alamos, New Mexico 87545, USA*
[3]*Materials and Process Simulation Center, California Institute of Technology, Pasadena CA 91125, USA*

(Received 3 November 2011; accepted 26 November 2011; published online 5 January 2012)

A useful synthesis technique, shock synthesis of bulk nanomaterials from nanopowders, is explored here with molecular dynamics simulations. We choose nanoporous Cu (~11 nm in grain size and 6% porosity) as a representative system, and perform consolidation and spallation simulations. The spallation simulations characterize the consolidated nanopowders in terms of spall strength and damage mechanisms. The impactor is full density Cu, and the impact velocity (u_i) ranges from 0.2 to 2 km s^{-1}. We present detailed analysis of consolidation and spallation processes, including atomic-level structure and wave propagation features. The critical values of u_i are identified for the onset plasticity at the contact points (0.2 km s^{-1}) and complete void collapse (0.5 km s^{-1}). Void collapse involves dislocations, lattice rotation, shearing/friction, heating, and microkinetic energy. Plasticity initiated at the contact points and its propagation play a key role in void collapse at low u_i, while the pronounced, grain-wise deformation may contribute as well at high u_i. The grain structure gives rise to nonplanar shock response at nanometer scales. Bulk nanomaterials from ultrafine nanopowders (~10 nm) can be synthesized with shock waves. For spallation, grain boundary (GB) or GB triple junction damage prevails, while we also observe intragranular voids as a result of GB plasticity. © *2012 American Institute of Physics*. [doi:10.1063/1.3675174]

I. INTRODUCTION

Shock compression of powders is a unique technique for materials synthesis.[1–9] For example, it allows consolidation of powders through rapid, localized energy deposition around the pores with less heating of the bulk materials,[9] thus preserving some desired material properties. Experimental and simulation/modeling efforts have been dedicated to shock consolidation for practical applications and for understanding the mechanisms. One application is synthesizing bulk nanomaterials from nanopowders (because nanopowders are widely available), including 50–70 nm Al nanopowders.[3,6,7] Molecular dynamics (MD) simulations of ultrafine nanopowder (~10 nm) consolidation are reasonably realistic and useful to help us gain insights into consolidation mechanisms.[1,4,9,10]

In this work, we perform MD simulations of shock-induced consolidation of nanopowders and their performance during subsequent tensile loading. We explore a model nanoporous system (cylindrical Cu nanopowders) and different impact velocities ($0.2 \le u_i \le 2$ km s^{-1}), and present detailed analysis of consolidation and spallation, including atomic-level structure and wave propagation features. The critical u_i values are identified for the onset plasticity at the contact points (stress concentrations) and full void collapse. Void collapse involves plastic flow, lattice rotation, shearing/friction, heating, and microkinetic energy (nanojetting). Plasticity initiated at the contact points and its propagation play a key role in void collapse at low u_i, while the pronounced, grain-wise deformation becomes important for high u_i. The grain structure gives rise to nonplanar shock response at nanometer scales. For spallation, grain boundary (GB) and GB triple junction damage prevails, while we also observe intragranular voids as a result of GB plasticity. Section II addresses the simulation methodology, followed by results and discussion in Sec. III, and summary in Sec. IV.

II. METHODOLOGY

Our MD simulations are performed using the Institut für Theoretische und Angewandte Physik (ITAP) Molecular Dynamics (IMD) code,[11] and an accurate embedded-atom-method potential.[12] We construct a nanoporous unit configuration, which contains six grains of identical shape and diameter (11.3 nm) within the three-dimensional (3D) periodic cell [Fig. 1(a)]. In our first attempt, we adopt cylindrical rather than spherical grains for simplicity. The columnar axis is along [100] (the rotation or *y*-axis; the transverse directions are along the *x*- and *z*-axes). There are three types of grains, each rotated by ±30° with respect to another. For each grain type, there are two identical grains in the unit configuration, and all the neighboring grains are of different grain types. The contact points *A*–*C* enclose a cylindrical pore; *A* and *B* are equivalent, where the stress concentration most likely occurs. The cross section of the pores is roughly triangular and the edge length is about 3.5 nm.

The microstructure unit (295 988 atoms) is relaxed at 0 K and thermalized at the ambient conditions with the constant-pressure-temperature ensemble and 3D periodic

a)Electronic mail: lihuang2002@hit.edu.cn.
b)Author to whom correspondence should be addressed. Electronic mail:sluo@lanl.gov.

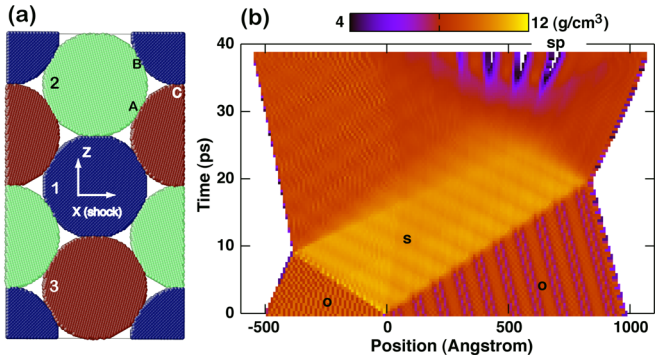

FIG. 1. (Color online) (a) The unit configuration of the nanoporous structure projected onto (100), consisting of three types of grains denoted as 1–3 (two grains for each type). *A*–*C* denote contact points between neighboring grains. (b) The *x*-*t* diagram in terms of density for an impact velocity $u_i = 1\,\mathrm{km\ s^{-1}}$. *O*: unshocked; *S*: shocked; *sp*: spall planes.

boundary conditions. The unit configuration is then replicated along the *x*-axis (shock direction) five times and equilibrated. The resulting configuration consists of 30 grains (1 479 940 atoms or $97.7\,\mathrm{nm} \times 5.7\,\mathrm{nm} \times 33.9\,\mathrm{nm}$ in edge lengths), and is the target in our shock simulations. The initial density of the nanoporous material is $\rho_0 = 8.29\,\mathrm{g\ cm^{-3}}$ (~94% full density). We also construct a full-density [100] flyer plate of the same cross-section but half the length of the target ($49.2\,\mathrm{nm} \times 5.7\,\mathrm{nm} \times 33.9\,\mathrm{nm}$; 818 176 atoms).

The flyer plate and the target are assembled along the *x*-axis (the flyer plate-target configuration; 2 298 116 atoms in total). The impact plane is located at $x = 0$. The flyer plate and target are assigned positive and negative initial velocities along the *x*-axis, respectively, before impacting each other; the velocity of the flyer plate relative to the target is the impact velocity, u_i, ranging from $0.2\,\mathrm{km\ s^{-1}}$ to $2\,\mathrm{km\ s^{-1}}$. We use the microcanonical ensemble in shock or impact simulations.[13] Periodic boundary conditions are applied along the *y*- and *z*-axes (not the *x*-axis or shock direction) to mimic 1D strain loading. The non-impact sides of the flyer plate and target are free surfaces. The time step for integrating the equations of motion is 1 fs, and the shock run durations are up to 50 ps.

We perform 1D and 2D binning analyses[14,15] to resolve spatially such physical properties as density (ρ), stress (σ_{ij}), particle velocity (u) and temperature (T) profiles at different stages of compression, release, and tension. (Averaging along the *y*-axis is applied for the 2D analysis.) The center-of-mass velocity of a bin is removed when we calculate T and σ_{ij} within each bin. The free surface velocity (u_{fs}) versus time (t) is obtained from the particle velocity evolution on the target free surface. We characterize the local deformation and local structure around an atom with the local von Mises shear strain (η^{vM})[16,17] and centrosymmetry parameter (CSP),[18] and use coordination number (CN) for visualizing voids.

The shock state or Hugoniot state parameters are obtained from the 1D profiles. The von Mises (shear) stress is defined as $\sigma^{\mathrm{vM}} = \sigma_{xx} - \frac{1}{2}(\sigma_{yy} + \sigma_{zz})$. The spall strength ($\sigma_{\mathrm{sp}}$), i.e., the maximum tensile stress, σ_{xx}, is evaluated in volume right before spallation in the spall zone from 1D or 2D analysis.

III. RESULTS AND DISCUSSION

We perform flyer plate impact simulations of consolidation and spallation of Cu nanopowders at $u_i = 0.2$, 0.3, 0.4, 0.5, 1, and $2\,\mathrm{km\ s^{-1}}$. For the high u_i cases ($u_i = 0.5$, 1, and $2\,\mathrm{km\ s^{-1}}$), the preexisting pores are completely filled by shock compression (except the pores near the free surface), yielding a hexagonal columnar nanocrystalline structure with GBs and GB triple junctions. Spallation occurs for $u_i \geq 1\,\mathrm{km\ s^{-1}}$. The atomic structure, wave propagation, and 1D and 2D binning analyses are presented in Figs. 1–10.

A. 1D analysis

The commonly used 1D binning analysis considers spatial variations only along the shock direction. The impact-induced shocks propagate in both directions (forward and backward), and are then reflected from the flyer plate and target free surfaces as release fans; their interaction in the target leads to decompression and then tension; spallation is induced when the tensile stress exceeds the spall strength σ_{sp}. This whole process is illustrated in the conventional *x*-*t* daigram [Fig. 1(b)]. Because 1D analysis lacks spatial resolution in the transverse directions, we only show a couple of examples.

Upon shock compression at $u_i = 0.5\,\mathrm{km\ s^{-1}}$ [Fig. 1(b)], the pore regions are compressed to higher densities (but still lower than the compressed, originally full density regions). The shock-compressed region shows periodic spatial variations directly related to the periodicity of the pores. Spallation is manifested in localized density reduction due to void nucleation, growth, and coalescence at spall planes, which are regularly spaced with the similar periodicity.

The rise time of the shock front in the free velocity histories [Fig. 2(a)] reflects the nonplanarity of the wave front due to structure heterogeneity, and the pore collapse dynamics. With increasing u_i, the rise time decreases (shock front steepens). The maximum tensile stress in relevant regions also increases and the tensile pulse shape varies [Fig. 2(b)]. Spallation induces local tensile stress relaxation and heating, and a recompression wave propagating toward the free surface, which produces the pullback in the free surface velocity histories. The 1D profiles indicate that spallation only occurs for the highest two impact velocities ($u_i \geq 1\,\mathrm{km\ s^{-1}}$). σ_{sp} is not necessarily the highest tensile stress region in the stress profiles because spallation may occur at weaker regions.

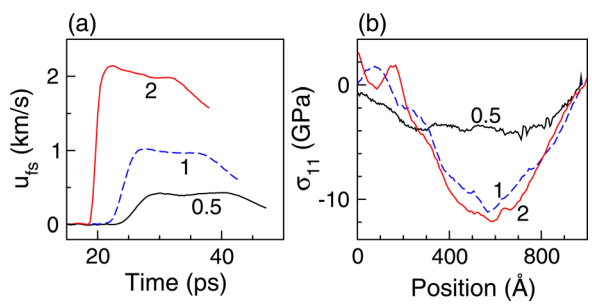

FIG. 2. (Color online) Free velocity histories, $u_{\mathrm{fs}}(t)$ (a); and stress profiles, $\sigma_{11}(x)$ (b) for different impact velocities (denoted by the numbers, in km $\mathrm{s^{-1}}$). $t = 46.4$, 38.4, and 32 ps for $u_i = 0.5$, 1, and $2\,\mathrm{km\ s^{-1}}$, respectively.

This is the case for $u_i = 1$ and 2 km s^{-1} [Fig. 2(b)], and σ_{sp} is about 9.6 GPa and 10.8 GPa, respectively, from the 1D analyses. For comparison, the maximum tensile stress achieved in the target is 11.2 GPa and 12.4 GPa, respectively. (See below for more discussions.)

Given the limitations of 1D binning analysis, we present below 2D binning analysis and 3D atomic configurations.

B. Deformation and nanopore collapse

Of particular interest are how the nanoporous Cu deforms and how nanopores collapse under shock compression. We show that the stress concentrations at the contact points in particular at *A* and *B* [Fig. 1(a)] induce plastic flow to fill in the pore volume. This process is dominant at low u_i. However, the rapid plastic flow within the grain interior, which is independent of the leading plastic flow originated at the stress concentration points, also contributes to or may prevail in the void collapse at high u_i (e.g., 2 km s^{-1}). Lattice rotation, shearing, and local friction; directional microkinetic energy deposition (nanojetting); and hotspots are also observed.

Figure 3 shows a snapshot of deformation and collapse of nanopores for $u_i = 0.5$ km s^{-1}, visualized with η^{vM}, CN, and CSP; the regular atoms are removed for clarity, and only defects or atoms undergoing certain local shear are shown. η^{vM} characterizes local shear regardless of its structural origin, e.g., apparent plasticity due to GB movement or conventional crystal plasticity [Fig. 3(a)]. The CN visualization in Fig. 3(b) shows dislocation loops, GBs, and other defects, but not stacking faults and twins (if any), because the atoms with CN $\neq$ 12 correspond to non-fcc or non-hcp atoms (fcc denotes face-centered cubic, and hcp, hexagonal close-packed). CSP reveals stacking faults or twins and other defects [Fig. 3(c)]. These three parameters are complementary and consistent in visualizing defects and deformation.

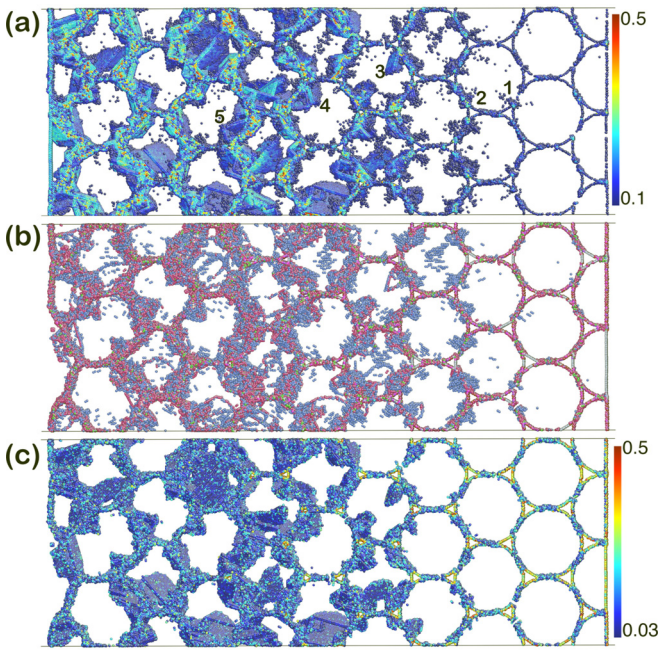

FIG. 3. (Color online) The atomic configuration at $t = 22$ ps for $u_i = 0.5$ km s^{-1}, visualized with Atomeye.[17] Color coding is based on local atomic shear strain (a), coordination number or CN (b; atoms with CN = 12 are not shown) and centrosymmetry parameter (c). Shock direction: left → right.

Behind the wave front, deformation increases at the contact points (types *A* and *B*) farther away from the wave front, as illustrated by the sequence 1-2-3-4-5 in Fig. 3(a); the nanopores become correspondingly smaller, and complete pore collapse occurs about five grains away from the wave front. The pore or void collapse is a direct result of the plastic flow initiated at the type *A* and *B* contact points. The nanoporous structure evolves into a deformed hexagonal columnar nanostructure after pore collapse, and the contact points extend into GBs (Fig. 3).

We also examine the grain movement as the compression wave traverses (Fig. 4; $u_i = 0.4$ km s^{-1}). Two pronounced features are observed: lattice rotation and local disordering. Lattice rotation is indicated by the curved, dashed lines; the lattices near the contact points are distorted and the atoms are commensurate across two different grains. On the other hand, atom movement is not commensurate across grains so local disordering, shearing, and friction (the circled area) is induced; as a result, dislocations emit from such high energy, disordered sites. Dislocation-mediated plastic flow is also the key mechanism in void collapse from single-void MD simulations.[19,20]

While void collapse is induced by plastic flow as shown above, such flow can be initiated from the contact points or other locations (e.g., grain interior), and the degree of void collapse may vary, depending the impact velocities. The compression responses for five selected cases ($u_i = 0.2$, 0.4, 0.5, 1, and 2 km s^{-1}) are compared in Figs. 3 and 5. At $u_i = 0.2$ km s^{-1}, only minor plasticity occurs at the type *A* and *B* contact points, the nanopowders remain elastic and void collapse is negligible [Fig. 5(a)]. With increasing u_i, the contact point plasticity increases, and the separation between the leading plastic deformation at the contact points and the relaxed state behind the wave front decreases (Fig. 5), consistent with the rise time feature in $u_{fs}(t)$ [Fig. 2(a)]. The contact point-initiated plasticity dominates the deformation and void collapse except for the case of 2 km s^{-1}. At this highest u_i case, the plastic deformation initiated within the grains immediately follows that at the contact points; the nucleation of

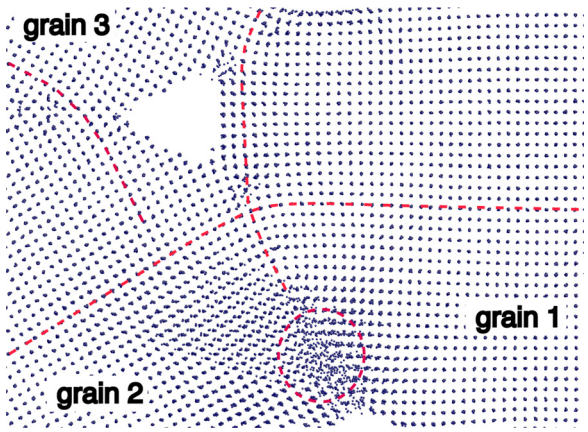

FIG. 4. (Color online) Atomic configuration showing lattice rotation (dashed curves) and disordering (circles), at $t = 14.8$ ps for $u_i = 0.4$ km s^{-1}. Shock direction: left → right.

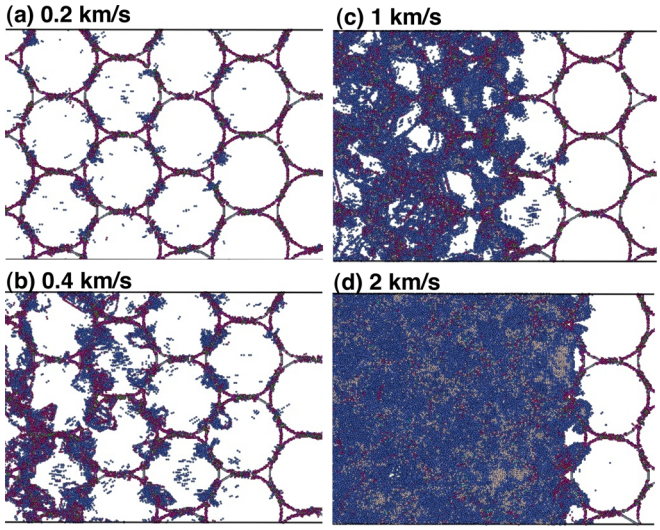

FIG. 5. (Color online) Snapshots of atomic configurations at $t = 14.8$ ps for different u_i, visualized with CN (atoms with CN = 12 are not shown). Shock direction: left → right.

the former is due to the strong compression loading and independent of the contact point plasticity. Partial void collapse is observed at 0.4 km^{-1} [Fig. 5(b)], and complete void collapse occurs at 0.5 km^{-1} (Fig. 3) and beyond [Figs. 5(c) and 5(d)]. For the void collapse at $u_i = 2$ km s^{-1}, the plastic flow originated from the grain interiors also contributes significantly to the collapse.

A key reason for the preferential nucleation of dislocations at the contact points (type *A* or *B*) is stress concentration. For example, the wave front shows pronounced, contact-point stress concentrations in $\sigma_{11}(x, z)$ [Fig. 6(a)]. Stress concentration in σ^{vM} also occurs but is highly transient due to rapid shear stress relaxation via deformation,

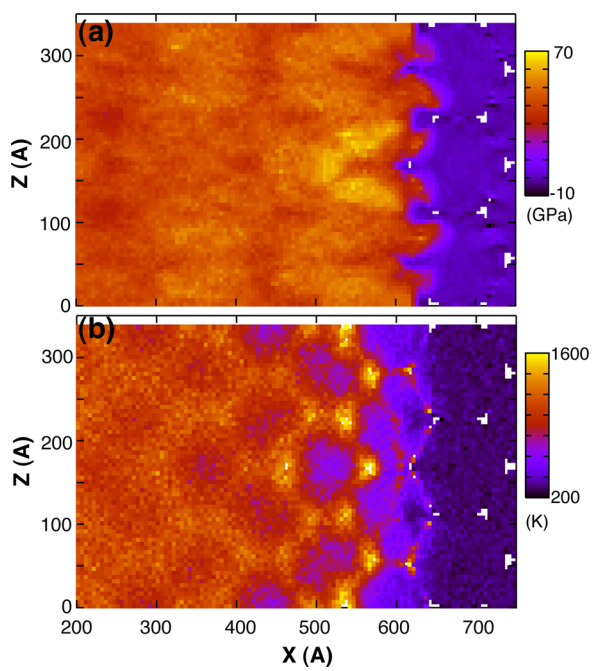

FIG. 6. (Color online) 2D profiles, $\sigma_{11}(x, z)$ and $T(x, z)$, at $t = 14.8$ ps for $u_i = 2$ km s^{-1}. Shock direction: left → right.

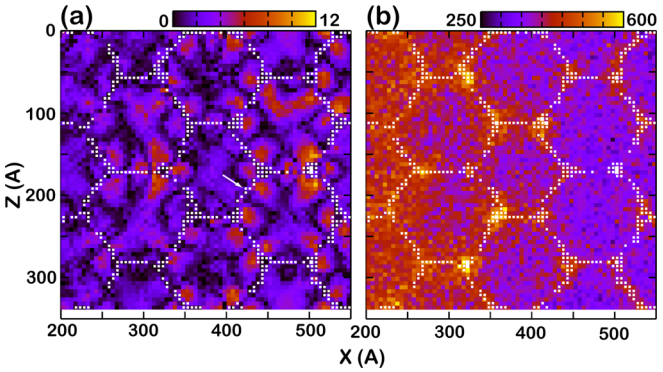

FIG. 7. (Color online) 2D profiles, $|\sigma^{vM}(x, z)|$ (a; in GPa) and $T(x, z)$ (b; in K) at $t = 22$ ps for $u_i = 0.5$ km s^{-1}, overlaid with the grain boundaries (white dots). Shock direction: left → right.

e.g., local disordering and dislocation emission [Figs. 3 and 7(a)]. Figure 7(a) shows the dynamics of σ^{vM} as manifested at different locations behind the wave front. The stress concentration locations are dynamic, e.g., the shear stress relaxation at the contact point may induce concentrations to shift along the GBs toward the pores, and the stress field becomes more homogeneous as relaxation behind the wave front progresses. This stress evolution [Fig. 7(a)] is consistent with the structure features (Fig. 3).

Both plastic deformation and void collapse itself induce local heating and thus hotspots. A portion of the mechanical work done by the void collapse (stress × local volume change) is converted to heat,[21] and this heating mechanism is likely dominant. Hotspots are observed for low and high impact velocities [Figs. 6(b) and 7(b)]. The hotspot dynamics do not necessarily follow those of stress and plastic deformation, e.g., we observe their delay relative to the stress wave front (Fig. 6). However, hotspot melting is not well expected in our simulation cases, if we compare the temperature with the melting curve,[22] although one could argue that melting may have occurred if the pressure is assumed to be close to zero near the nanopores. But the void collapse is highly transient and local heat conduction is not negligible, so melting is not well defined in our cases. The temperature field also becomes homogenized behind the shock front. As a result, the average shock temperature is elevated by the void collapse, e.g., by about 400 K for $u_i = 2$ km s^{-1} or ~43 GPa. (The shock temperature for solid density Cu is about 700 K at this pressure.[22])

The presence of pores may lead to directional microkinetic energy deposition during void collapse,[1] and nanojetting may occur. For the highest impact energy simulated (2 km s^{-1}), the highest particle velocity spots are located in the nanopores during their collapse (Fig. 8). However, further growth of the nanojets is impeded by the small pore size and pore collapse.

C. Nonplanar shock and surface roughening

The microstructure inherent in the nanoporous Cu, including nanopores and grain boundaries, gives rise to pronounced deviation of the shock front from perfect planarity, which in turn may induce, for example, instability growth

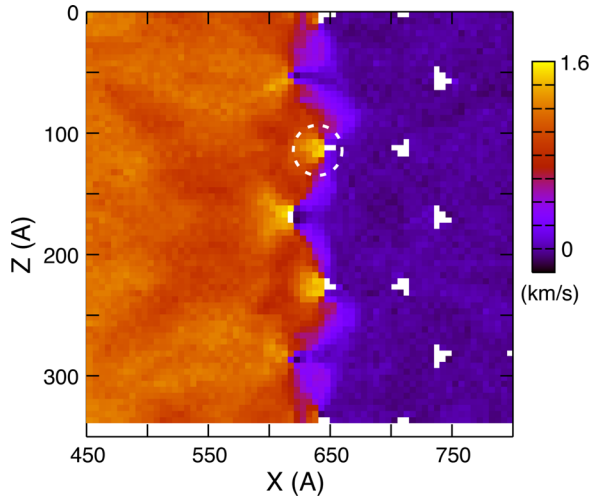

FIG. 8. (Color online) 2D velocity profile $u_x(x, z)$ at $t = 14.8$ ps for $u_i = 2$ km s^{-1}. u_x is corrected for the initial velocity. High velocity spots (e.g., the circled area) are located in the pores. Shock direction: left → right.

upon encountering interfaces downstream. We thus examine nonplanarity in the in-volume profiles and free surface roughness (e.g., Figs. 5–9).

For cross-sections parallel to the shock direction, density and wave speed are the highest on those traversing contact points *A* and *B*, and the lowest on those crossing contact point *C* [Fig. 1(a)]. (Stress concentration also occurs at contact points *A* and *B*.) This wave speed difference along the *z*-direction is one cause for the nonplanarity of the shock front; wave scattering, stress concentration, grain deformation, and anisotropy may contribute as well. The nonplanarity of shock front is manifested in deformation (Fig. 5), and 2D profiles of particle velocity, stress, and temperature (Figs. 6–8), although the exact features are different. The plastic deformation front (Fig. 5) and the leading stress wave front in $\sigma_{xx}(x, z)$ [Fig. 6(a)] are direct results of the stress concentrations. A two-wave structure is observed in $u_x(x, z)$ (Fig. 8). The precursor appears to be the direct result of wave speed difference along *x*, and the profile is smeared. The second wave front in $u_x(x, z)$ largely follows the grain

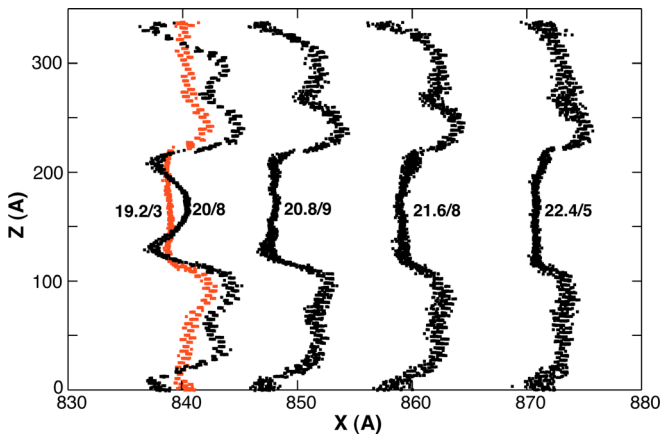

FIG. 9. (Color online) Target free surface roughening during and after shock breakout, for $u_i = 2$ km s^{-1}. The number pairs (e.g., 19.2/3) denote time in ps/surface roughness in Å. The latter is simply defined as the peak-trough value. Shock direction: left → right.

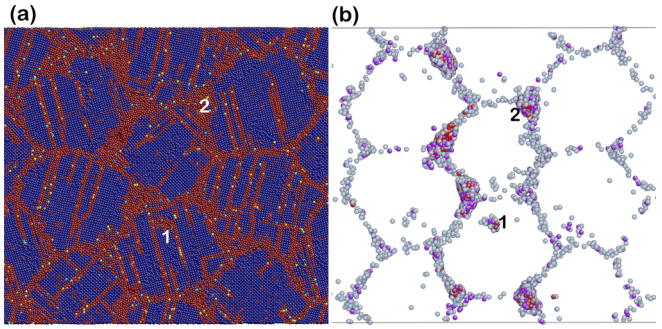

FIG. 10. (Color online) Snapshots of deformation (a) and void nucleation (b) at $t = 40$ ps for $u_i = 1$ km s^{-1}, projected along the *y*-direction. CSP and CN are used for visualization in (a) and (b), respectively. Only undercoordinated atoms with CN ≤ 8 are shown in (b). Shock direction: left → right.

geometry, and the leading positions correspond to the particular pores similar to those enclosed by *ABC* in Fig. 1(a), which are more susceptible to jetting as discussed above. The $T(x, z)$ front is delayed related to that in $\sigma_{11}(x, z)$, and the main roughening feature in the $T(x, z)$ front is related to hotspot formation at pores [Fig. 6(b)].

Shock-induced surface roughening due to microstructure was observed in experiments[23] and MD simulations of nanolaminates.[24] We follow the target free surface movement after shock breakout. Figure 9 shows the dynamics of free surface for $u_i = 2$ km s^{-1}. Shock breaks out in the top and bottom grains first, so the free surface of the center grain remains flat while the rest undergoes roughening ($t = 19.2$ ps). The arrival of the leading wave in the center grain free surface induces its roughening (20 ps), but this local roughening is reduced due to drag by the faster movement of the free surfaces of the top and bottom grains (20.8 ps). The overall roughening peaks at 20.8 ps (9 Å) and then decreases due to further wave interactions (21.6 and 22.4 ps). The free surface shape and roughening continue to evolve dynamically. However, the grain size affects the roughening in the volume and on the free surface, and this effect remains to be explored.

D. Spallation

During release, the compression-induced deformation (e.g., stacking faults) may be partially reversed. The interactions of the release fans lead to tension. Plastic deformation then increases during tension, and spallation occurs at sufficient shock strength (Fig. 10). Figure 10(a) shows GB-related deformation: copious stacking faults, some microtwins, and other defects. The *x-t* diagram in Fig. 1(b) obtained from 1D analysis suggests that spall planes are regularly spaced. The atomic configurations during tension [e.g., Fig. 10(b)] reveal that voids predominantly nucleate near the GB triple junctions, and grow and coalesce along the GBs. The spall planes in Fig. 1(b) thus correspond to the spalled GBs.

The spall strength is normally defined as the maximum tensile stress in the 1D stress profiles, $\sigma_{11}(x)$ [Fig. 2(b)]; however, the region with maximum tensile stress does not necessarily correspond to the GB region where spall occurs.

2D stress profiles are more appropriate for defining σ_{sp}. For $u_i = 1$ and 2 km s^{-1}, σ_{sp} is about 6–8 GPa in GBs and GB triple junctions from 2D stress profiles. σ_{sp} is significantly lower than that for columnar nanocrystalline forms without preexisting nanopores,[15] due to the pronounced heating effect associated with pore collapse. (We do not expect release melting, though, if we compare the prespall temperature with the melting curve in the tensile regime.[14] The temperature is homogenized during tension, and the GBs are also preserved even at $u_i = 1$ km s^{-1}, so melting is unlikely.) However, σ_{sp} is still high (indicating high degree of consolidation); the extremely high strain rates in such conventional MD simulations may also play a role.

Although voids are nucleated primarily near GB triple junctions [e.g., 2 in Fig. 10(b)], we observe occasionally *apparent* intragranular void nucleation [1 in Fig. 10(b)]. This void nucleation is not independent of the GBs, because it is due to the interaction of dislocations emitted from GBs [Fig. 10(a)]. The weakening effect of dislocation interaction and intersecting[25,26] was also observed previously and we argued that such void nucleation is still intergranular in nature,[15] because it occurs in the GB-affected zone[27] and is a direct result of GB deformation.

As shown above, the tensile stress can be significant and induce damage to the consolidated powders. Tensile loading should be minimized for the experiments designed for synthesizing bulk shock-consolidated nanopowders, and proper choice of radial and longitudinal momentum traps can reduce such damage.

Our simulations of nanoporous Cu demonstrate that void collapse is achieved via plastic flow initiated from stress concentration points or grain interiors, and involves lattice rotation, shearing, and friction; hotspot formation; and nanojetting. These observations agree largely with previous qualitative description of the collapse mechanism[1] and continuum modeling.[9] Our MD simulations reveal rich, detailed deformation and collapse mechanisms. However, it remains to explore the rate, size, and microstructure effects in order to develop practical models for consolidation of powder materials.

IV. CONCLUSION

We have performed MD simulations of consolidation of nanoporous Cu, and characterized the dynamic tensile response of the consolidated nanopowders. The critical values of u_i are identified for the onset plasticity at the contact points (0.2 km s^{-1}) and full void collapse (0.5 km s^{-1}). Void collapse involves dislocations, lattice rotation, shearing, and friction; heating; and microkinetic energy (nanojetting). Plasticity initiated at the contact points and its propagation play a key role in void collapse at low u_i, while the pronounced, grain-wise deformation may contribute as well at high u_i. The grain structure gives rise to nonplanar shock response at nanometer scales (shock front and surface roughening). Full consolidation of ultrafine nanopowders appears feasible. For spallation, GB or GB triple junction damage prevails, while we also observe intragranular voids as a result of GB plasticity.

ACKNOWLEDGMENTS

This work is supported by Natural Science Foundation of China under Grant No. 10904023 (L.H.), and the PSAAP project at Caltech (Q.A. and W.A.G.). Los Alamos National Laboratory (LANL) is operated by Los Alamos National Security, LLC for the U.S. Department of Energy (DOE) under contract No. DE-AC52-06NA25396.

[1] M. A. Meyers, *Dynamic Behavior of Materials* (Wiley, New York, 1994).
[2] N. N. Thadhani, Prog. Mater. Sci. **37**, 117 (1993).
[3] V. Viswanathan, T. Laha, K. Balani, A. Agarwal, and S. Seal, Mater. Sci. Eng. Rep. **54**, 251 (2006).
[4] W. H. Gourdin, J. Appl. Phys. **55**, 172 (1984).
[5] R. B. Schwarz, P. Kasiraj, T. Vreeland Jr., and T. J. Ahrens, Acta Metall. **32**, 1243 (1984).
[6] T. G. Nieh, P. Luo, W. Nellis, D. Lesuer, and D. Benson, Acta Mater. **44**, 3781 (1996).
[7] Z. Q. Jin, K. H. Chen, J. Li, H. Zeng, S. F. Cheng, J. P. Liu, Z. L. Wang, and N. N. Thadhani, Acta Mater. **52**, 2147 (2004).
[8] T. Akashi and A. B. Sawaoka, J. Mater. Sci. **22**, 3276 (2003).
[9] R. L. Williamson and R. A. Berry, in *Shock Compression of Condensed Matter–1985*, edited by Y. M. Gupta (Plenum, New York, 1986), p. 341.
[10] W. Hermann, J. Appl. Phys. **40**, 2490 (1969).
[11] J. Stadler, R. Mikulla, and H.-R. Trebin, Int. J. Mod. Phys. C **8**, 1131 (1997).
[12] Y. Mishin, M. J. Mehl, D. A. Papaconstantopoulos, A. F. Voter, and J. D. Kress, Phys. Rev. B **63**, 224106 (2001).
[13] B. L. Holian, Shock Waves **5**, 149 (1995).
[14] S. N. Luo, Q. An, T. C. Germann, and L. B. Han, J. Appl. Phys. **106**, 013502 (2009).
[15] S. N. Luo, T. C. Germann, T. G. Desai, D. L. Tonks, and Q. An, J. Appl. Phys. **107**, 123507 (2010).
[16] F. Shimizu, S. Ogata, and J. Li, Mater. Trans. **48**, 2923 (2007).
[17] J. Li, Modell. Simul. Mater. Sci. Eng. **11**, 173 (2003).
[18] C. L. Kelchner, S. J. Plimpton, and J. C. Hamilton, Phys. Rev. B **58**, 11085 (1998).
[19] W. J. Zhu, Z. F. Song, X. L. Deng, H. L. He, and X. Y. Cheng, Phys. Rev. B **75**, 024104 (2007).
[20] L. P. Davila, P. Erhart, E. M. Bringa, M. A. Meyers, V. A. Lubarda, M. S. Schneider, R. Becker, and M. Kumar, Appl. Phys. Lett. **86**, 161902 (2005).
[21] Ya. B. Zel'dovich and Yu. P. Raizer, *Physics of Shock Waves and High-Temperature Hydrodynamic Phenomena* (Dover, Mineola, NY, 2002).
[22] Q. An, S. N. Luo, L.-B. Han, L. Q. Zheng, and O. Tschauner, J. Phys.: Condens. Matter **20**, 095220 (2008).
[23] D. L. Paisley, S. N. Luo, S. R. Greenfield, and A. C. Koskelo, Rev. Sci. Instrum. **79**, 023902 (2008).
[24] S. N. Luo, T. C. Germann, D. L. Tonks, and Q. An, J. Appl. Phys. **108**, 093526 (2010).
[25] S. N. Luo, T. C. Germann, and D. L. Tonks, J. Appl. Phys. **106**, 123518 (2009).
[26] S. G. Srinivasan, M. I. Baskes, and G. J. Wagner, J. Appl. Phys. **101**, 043504 (2007).
[27] P. Peralta and C. Laird, Acta Mater. **45**, 3029 (1997).